Monthly Notices
of the
ROYAL ASTRONOMICAL SOCIETY

MNRAS **495,** 2844–2857 (2020)
Advance Access publication 2020 May 14

doi:10.1093/mnras/staa1337

Mode identification in three pulsating hot subdwarfs observed with *TESS* satellite

S. K. Sahoo [1,2★] A. S. Baran [1] U. Heber,[3] J. Ostrowski [1] S. Sanjayan,[1,2] R. Silvotti [4] A. Irrgang,[3] M. Uzundag,[5,6] M. D. Reed [1,7] K. A. Shoaf,[7] R. Raddi [3,8] M. Vuckovic,[5] H. Ghasemi [9] W. Zong[10] and K. J. Bell[11†]

[1]*ARDASTELLA Research Group, Institute of Physics, Pedagogical University of Krakow, ul. Podchorążych 2, PL-30-084 Kraków, Poland*
[2]*Nicolaus Copernicus Astronomical Centre of the Polish Academy of Sciences, ul. Bartycka 18, PL-00-716 Warsaw, Poland*
[3]*Dr. Remeis-Sternwarte and ECAP, Astronomical Institute, University of Erlangen-Nürnberg, Sternwartstr. 7, D-96049 Bamberg, Germany*
[4]*INAF – Osservatorio Astrofisico di Torino, Strada dell'Osservatorio 20, I-10025 Pino Torinese, Italy*
[5]*Instituto de Fisica y Astronomia, Facultad de Ciencias, Universidad de Valparaiso, Gran Bretana 1111, Playa Ancha 2360102, Valparaiso, Chile*
[6]*European Southern Observatory, Alonso de Cordóva 3107, Santiago, Chile*
[7]*Department of Physics, Astronomy, and Materials Science, Missouri State University, Springfield, MO 65897, USA*
[8]*Departament de Fisica, Universitat Politecnica de Catalunya, c/ Esteve Terrades 5, E-08860 Castelldefels, Spain*
[9]*Department of Physics, Institute for Advanced Studies in Basic Sciences (IASBS), Zanjan 45137-66731, Iran*
[10]*Department of Astronomy, Beijing Normal University, Beijing 100875, PR China*
[11]*DIRAC Institute, Department of Astronomy, University of Washington, Seattle, WA 98195-1580, USA*

Accepted 2020 May 7. Received 2020 May 5; in original form 2020 March 23

ABSTRACT

We report on the detection of pulsations of three pulsating subdwarf B stars observed by the *Transiting Exoplanet Survey Satellite (TESS)* satellite and our results of mode identification in these stars based on an asymptotic period relation. SB 459 (TIC 067584818), SB 815 (TIC 169285097), and PG 0342 + 026 (TIC 457168745) have been monitored during single sectors resulting in 27 d coverage. These data sets allowed for detecting, in each star, a few tens of frequencies that we interpreted as stellar oscillations. We found no multiplets, though we partially constrained mode geometry by means of period spacing, which recently became a key tool in analyses of pulsating subdwarf B stars. Standard routine that we have used allowed us to select candidates for trapped modes that surely bear signatures of non-uniform chemical profile inside the stars. We have also done statistical analysis using collected spectroscopic and asteroseismic data of previously known subdwarf B stars along with our three stars. Making use of high precision trigonometric parallaxes from the *Gaia* mission and spectral energy distributions we converted atmospheric parameters to stellar ones. Radii, masses, and luminosities are close to their canonical values for extreme horizontal branch stars. In particular, the stellar masses are close to the canonical one of 0.47 $M_{\odot}$ for all three stars but uncertainties on the mass are large. The results of the analyses presented here will provide important constrains for asteroseismic modelling.

Key words: asteroseismology – stars: oscillations (including pulsations) – subdwarfs.

1 INTRODUCTION

Subdwarf B (sdB) stars are extreme horizontal branch stars, consist of a convective helium burning core, helium shell and a very thin (in mass) hydrogen envelope. The effective temperatures $T_{\rm eff}$ are in a range of 20 000–40 000 K, which moved them blueward from the normal horizontal branch stars in the Hertzsprung–Russell diagram (Heber 2016). The sdB stars are found in almost all stellar populations, field (Altmann, Edelmann & de Boer 2004; Martin et al. 2017) as well as open (Kaluzny & Ruciński 1993) and globular clusters (Moehler 2001; Moni Bidin et al. 2008). The sdB stars have masses nearly 0.5 $M_{\odot}$ and surface gravities, in a logarithmic scale, $\log(g/\,{\rm cm\,s^{-2}})$ of 5.0 – 5.8 (Heber 2016), which means that they are compact in size (0.15 – 0.35 $R_{\odot}$). They are considered to be one of the most ionizing sources of interstellar gas at high galactic latitudes (de Boer 1985), and mostly responsible for

★ E-mail: sumanta.kumar27@gmail.com
† NSF Astronomy and Astrophysics Fellow.

Table 1. Basic information of the targets. First rows for each target refer to the parameters used in our work. Additional references are given for comparison.

TIC	Name	Sectors	$T_{\rm eff}$ (K)	$\log g/({\rm cm\,s^{-2}})$	$\log n_{\rm He}/n_{\rm H}$	Gmag	Distance (pc)	Reference for $T_{\rm eff}$ and $\log g$
067584818	SB 459	3	24 900(500)	5.35(10)	− 2.58(10)	12.2	422(12)	**This work**
			25 000(1200)	5.30(20)	− 2.8(30)			Heber et al. (1984)
169285097	SB 815	2	27 200(550)	5.39(10)	− 2.94(01)	10.9	246(5)	Schneider et al. (2018)
			28 800(1500)	5.40(20)	− 2.46(30)			Heber et al. (1984)
			28 390(300)[a]	5.39(04)[a]	− 3.07(24)[a]			Németh, Kawka & Vennes (2012)
			27 000(1100)	5.32(0.12)	− 2.90(10)			Geier et al. (2013)
457168745	PG 0342 + 026	5	26 000(1100)	5.59(12)	− 2.69(10)	10.9	163(3)	Geier et al. (2013)
			26200(1000)	5.67(15)	− 2.4(15)			Saffer et al. (1994)

[a]Symmetric errors are given instead of the original asymmetric ones. Systematic errors are not accounted for.

the ultraviolet upturn phenomenon in early-type galaxies (Brown et al. 1997).

Due to a low mass of the hydrogen envelope ($<10^{-2}\,M_{\odot}$), sdB stars are not able to sustain two shell nuclear burning, skipping the asymptotic giant branch, and heading directly to the white dwarf cooling track, right after the helium in the core is exhausted. The reason for the lack of a more massive hydrogen envelope is still a puzzle, though binarity is a natural explanation for a mass-loss. This can explain sdBs in binaries. A merger event can be invoked as a channel leading to formation of single sdBs (Han et al. 2002). According to Charpinet et al. (2018) who presented results on stellar rotation analysis, substellar companions may also be responsible for mass-loss, while the objects are still observationally single. Fontaine et al. (2012) concluded that the mass distribution points at single star evolution, however in those cases a strong wind is necessary to remove the hydrogen envelope. No evidence for a strong wind has been reported thus far.

Discovery of pulsating sdB stars (hereafter: sdBV) by Kilkenny et al. (1997) has opened a way to understand their internal structure by using asteroseismological techniques (Charpinet et al. 1997). SdBV stars show pulsations in p modes or g modes, though a mix of the modes are recently commonly found in the so-called hybrid sdBV stars. Typical periods of p-mode pulsators are of the order of minutes, while periods of g-mode pulsators are of the order of hours (Heber 2016).

In the field of sdBV stars, a significant improvement has been made during the last several years and a big credit goes to the Kepler and K2 missions due to their unprecedented data delivery. Asteroseismic analyses of Kepler-observed sdBV stars have revealed interesting and useful features. Rotationally split multiplets and asymptotic period sequences have never been easy to detect in ground-based data; Balloon 090100001 being an exception (Baran et al. 2009). Multiplets allowed for identification of low degree ($\ell \leq 2$) modes, although higher degrees ($3 \leq \ell \leq 8$) in the 'intermediate region' of 400–700 μHz have been also detected (Telting et al. 2014; Foster et al. 2015; Silvotti et al. 2019). An observed period spacing between consecutive overtones of g modes of the same modal degree, ranges from 230 to 270 s (Reed et al. 2018a). Asymptotic sequences often show a 'hook' feature (e.g. Baran & Winans 2012) in échelle diagrams and occasionally include trapped modes (e.g. Østensen et al. 2014), which is likely the indication of a non-uniform chemical profile along a stellar radius (Charpinet et al. 2000). Pulsation models also predict low order p-mode overtones to be spaced in frequency by 800–1100 μHz (Charpinet et al. 2000). Observations have yielded a mixture of results, with three sdBV stars in agreement (Baran et al. 2009; Foster et al. 2015; Reed et al. 2018b) and two other with much smaller spacings (Baran et al. 2012; Reed et al. 2018b).

The successor of Kepler and K2 missions, Transiting Exoplanet Survey Satellite (*TESS*; Ricker et al. 2014), an all-sky survey, satellite has been launched on 2018 April 18. The main goal of the *TESS* mission is to detect exoplanets around nearby bright (down to about 15 mag) stars by using the transit method. It provides data over a time span of 2 yr by using its four CCD cameras with 24 × 96 deg field of view, which is known as an individual sector. *TESS* will cover 26 sectors over 24 months. The short cadence (SC) mode of 2 min, allocated for a selected sample of targets, allows us to investigate the light variations of the pulsating subdwarf B stars, covering entire g-mode region and reaching up to the longest period p modes.

This paper reports results of our work on three sdB stars monitored during the *TESS* mission and found to be light variable consistent with stellar pulsations. The targets SB 459 (TIC 067584818) and SB 815 (TIC 169285097) have been first identified by Slettebak & Brundage (1971) as early-type stars near the Southern Galactic pole and classified as sdB stars by Graham & Slettebak (1973). Both stars have been studied by the Montreal-Cambridge-Tololo survey as MCT 0106 − 3259 and MCT 2341 − 3443 (Lamontagne et al. 2000). PG 0342 + 026 (TIC 457168745) was discovered by the Palomar Green survey to be a sdB star (Green, Schmidt & Liebert 1986). Østensen et al. (2010) were first attempting at finding pulsations in SB 815. Unluckily, due to a short run, no variability has been reported. Another attempt was done using the SuperWASP telescope and (Holdsworth et al. 2017) detected pulsations, marking the star as an sdBV.

We use Fourier technique to detect frequencies and asymptotic period spacings to identify pulsation modes and follows the first paper in our series (Charpinet et al. 2019). The work is a continuation of our effort started with the advent of the Kepler and K2 missions.

2 SPECTROSCOPIC ANALYSIS

Atmospheric parameters of SB 815 and PG 0342 + 026 are available in the recent literature and are presented in Table 1 along with our determination of these parameters of SB 459. We also determined the radial velocities of PG 0342 + 026, which is explained in details below.

In case of SB 459, the only available quantitative spectral analysis was carried out by Heber et al. (1984). Therefore, it was considered worthwhile to revisit the star and to take another spectrum with more advanced instruments than before. The ESO Faint Object Spectrograph and Camera 2 (EFOSC2) spectrograph at the 3.58-m New Technology Telescope (NTT) at the La Silla Observatory was used. The single spectrum was obtained on 2019 June with grism #7, a slit of 1 arcsec covering the wavelength range from 3270 to 5240 Å. Given that we used 2 × 2 binning the nominal resolution of the

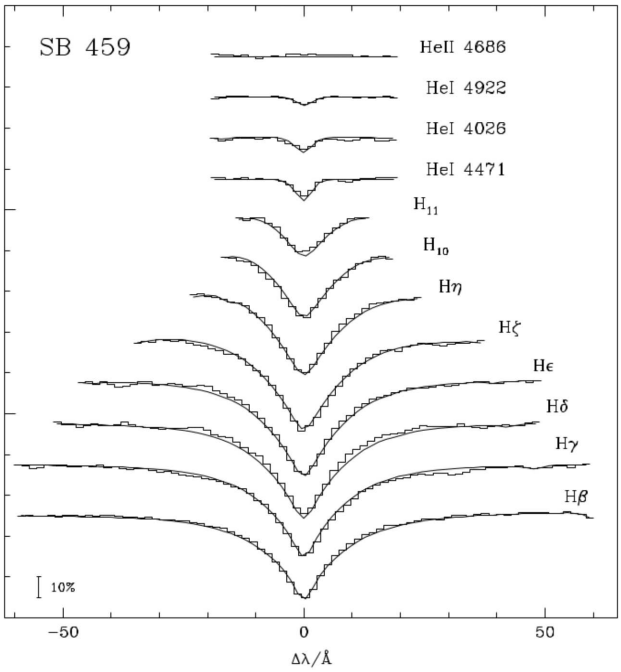

Figure 1. Spectral line fit of the Dupont spectrum of SB 459.

spectrum should be $\Delta\lambda \sim 6.4$ Å. However, the seeing was excellent such that the slit was underfilled, which resulted in somewhat better resolution of 5.4 Å as measured directly from the spectrum. The exposure time was 350 s. We reduced the long-slit spectra using standard IRAF packages (Tody 1986, 1993), by performing bias-subtraction, flat-field correction, wavelength, and flux calibrations (Massey, Valdes & Barnes 1992; Massey 1997). The observed standard star was Feige 110. The final spectrum has a signl-to-noise ratio of ~ 300 at 4200 Å.

SB 459 was also observed with Boller & Chivens Spectrograph at the 2.5-m Iréné Du Pont Telescope at the Las Campanas Observatory. The single spectrum was taken on 2019 October 31 using the following instrument setup, the grating of 600 lines mm^{-1} corresponding to the central wavelength of 5000 Å covering a wider wavelength range from 3427 to 6573 Å. We used a slit width of 1 arcsec which resulted in somewhat better resolution, than EFOSC2, of $\Delta\lambda \sim 3.1$ Å. For the data reduction, we followed the same steps as in the case EFOSC2 spectra. The signal-to-noise ratio of the final spectrum is ~ 250 at 4200 Å with 600 s exposure time.

We matched eight Balmer lines and four He I lines to both the EFOSC and the Dupont spectrum (Fig. 1) with the metal-line blanketed LTE grid of Heber, Reid & Werner (2000) using χ^2 minimization techniques as described in Napiwotzki, Green & Saffer (1999). The error budget is dominated by systematic errors, which we estimate at 2 per cent for the effective temperature and ±0.1 dex for the surface gravity (see Schneider et al. 2018). The resulting atmospheric parameters are remarkably similar at $T_{\rm eff} = 25\,100$ K, $\log g/({\rm cm\,s^{-2}}) = 5.34$, $\log n_{\rm He}/n_{\rm H} = -2.61$ for the EFOSC spectrum and $T_{\rm eff} = 24\,700$ K, $\log g/({\rm cm\,s^{-2}}) = 5.36$, $\log n_{\rm He}/n_{\rm H} = -2.55$ for the Dupont spectrum. We adopted the mean values as listed in Table 1, which agree with the published values to within respective error limits.

PG 0342 + 026 was observed in 2012 November–December with Harps-N at the Telescopio Nazionale Galileo (TNG, La Palma) in the context of a program to search for sdB low-mass companions

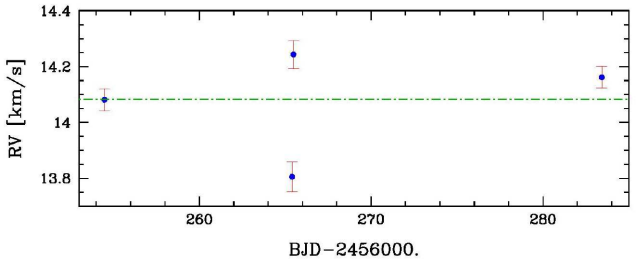

Figure 2. Radial velocities of PG 0342 + 026. Although four measurements are not enough to fit the RV data with the main pulsation frequencies, at least they give a rough estimate of the RV amplitudes involved.

(see Silvotti, Ostensen & Telting 2019 for more details). Four high-resolution spectra were collected with a mean signal-to-noise ratio of 71 at 4700 Å.[1] Using the cross-correlation function on about 150 absorption lines (excluding H and He lines that are too broad), we computed the radial velocities (RV) of the star and we found a mean system velocity of $+14.07$ km s^{-1} with significant variations around this value (Fig. 2). Thanks to the *TESS* observations, we can now confirm that these variations are at least partly caused by g-mode pulsations, as it has been suspected since 2012. Having available only four RV data points, and knowing that this star pulsates in at least 20 frequencies, we are unable to obtain a reliable fit, however, these data can be used to derive an upper limit to the minimum mass ($M \sin i$) of a hypothetical companion. The question whether this sdB star is single or not is important for its evolution prior to EHB.

In order to set upper limits to the mass of a companion, we computed a series of synthetic RV curves for different orbital periods and companion masses, assuming circular orbits, and compared these curves with the RV measurements. For each synthetic RV curve we selected the phase that gives the best fit to the data using a weighted least-squares algorithm. For each observational point we computed the difference, in absolute value and in σ units (where σ is the observation error), between observed and synthetic RV values. The colour coding in Fig. 3 corresponds to the mean value of this difference in σ units. We should keep in mind, however, that these upper limits to the mass of a companion are likely overestimated given that most if not all the variations that we see in Fig. 2 are likely caused by pulsations.

3 SPECTRAL ENERGY DISTRIBUTION, INTERSTELLAR REDDENING, AND STELLAR PARAMETERS

Photometric measurements allow the angular diameters to be determined along with the interstellar extinction, once the atmospheric parameters are known. We constructed spectral energy distributions from photometric measurements ranging from the ultraviolet (*IUE*) to the infrared. Infrared data were taken from 2MASS, VISTA-VIKING (J, H, K; Skrutskie et al. 2006), and *WISE* ($W1$, $W2$, Cutri & et al. 2012) catalogues. Magnitudes and colours in the Johnson (Allard et al. 1994; Mermilliod, Mermilliod & Hauck 1997; Landolt 2007), Strömgren (Wesemael et al. 1992; Paunzen 2015), APASS (Henden et al. 2015), SkyMapper (Wolf et al. 2018), and *Gaia* (Gaia Collaboration 2018) photometric systems were fitted (for details

[1]These spectra show a large number of metal absorption lines, many of which do not yet have a certain identification. The line identification is in progress and the results will be presented in a subsequent article.

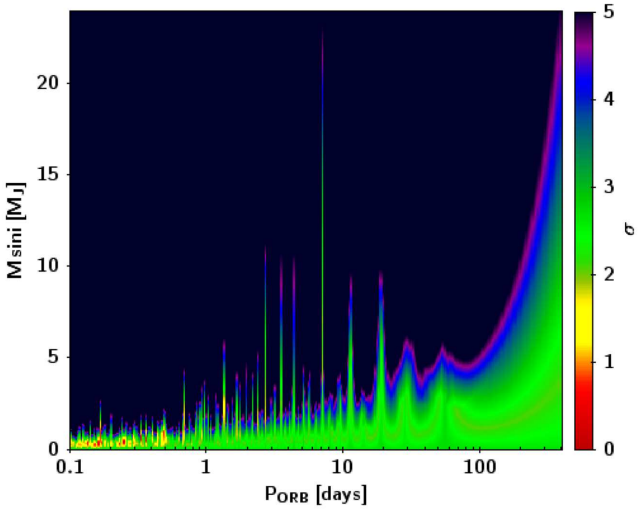

Figure 3. Upper limits to the mass of a hypothetical companion to PG 0342 + 026 as a function of orbital period. The regions where the presence of a companion is more compatible with the RV measurements are those in red/yellow/green, while the regions in dark blue correspond to a very low probability to have a companion. See text for more details.

see Heber, Irrgang & Schaffenroth 2018). Three numerical box filters were defined to derive UV-magnitudes from *IUE* UV spectra covering the spectral ranges 1300–1800, 2000–2500, and 2500–3000 Å. Interstellar extinction is accounted for using the extinction curve of Fitzpatrick (1999).

The angular diameter and the interstellar reddening parameter $E(B-V)$ were the only free parameter in the matching of the synthetic the SEDs to the observed ones. In Fig. 4, we plot the SEDs as flux density times the wavelength to the power of three ($F_\lambda \lambda^3$) versus the wavelength to reduce the steep slope of the SED over such a broad wavelength range. We also display the residuals (O–C) of the magnitudes and the colours. The synthetic SEDs match the observed ones very well in all parts of the wide spectral range. Hence, there is no contribution from potential companions at any wavelength for all three stars. Interstellar reddening is consistent with zero for SB 459 and SB 815 and small for PG 0342 + 026, all in accordance with the predictions of the maps of Schlegel, Finkbeiner & Davis (1998) and Schlafly & Finkbeiner (2011). The resulting angular diameters and interstellar reddening parameters are given in Tables 2, 3, and 4.

In its second data release the *Gaia* mission (Gaia Collaboration 2018) provided trigonometric parallaxes of high precision (to better than 3 per cent) for all three stars. The 'renormalized unit weight error' (RUWE; see Lindegren 2018) is a good quality indicator for the astrometric solution, because it is independent of the colour of the object. This makes it the best choice to judge the quality of the *Gaia* parallaxes of blue stars, such as studied here. The RUWE value is below the recommended value of 1.4 for all three stars, indicating that the astrometric solutions are reliable. The *Gaia* parallaxes and the angular diameters allow us to convert the atmospheric parameters to stellar radii via $R_\star = \Theta/(2\varpi)$, masses via $M_\star = gR_\star^2/G$, and luminosities via $\log\left(\frac{L}{L_\odot}\right) = \log\left(\left(\frac{R_\star}{R_\odot}\right)^2 \left(\frac{T_{\rm eff}}{5775\,{\rm K}}\right)^4\right)$. The results are summarized in Tables 2, 3, and 4. Uncertainties of the derived radii and luminosities are small because of the high precision of the *Gaia* parallaxes and well-constrained effective temperatures. The derived masses, however, have larger uncertainties resulting from the uncertainties of the spectroscopic surface gravities. The resulting masses are close to canonical (Dorman, Rood & O'Connell 1993), but uncertainties are large, mainly due to the surface gravity not yet being sufficiently constrained.

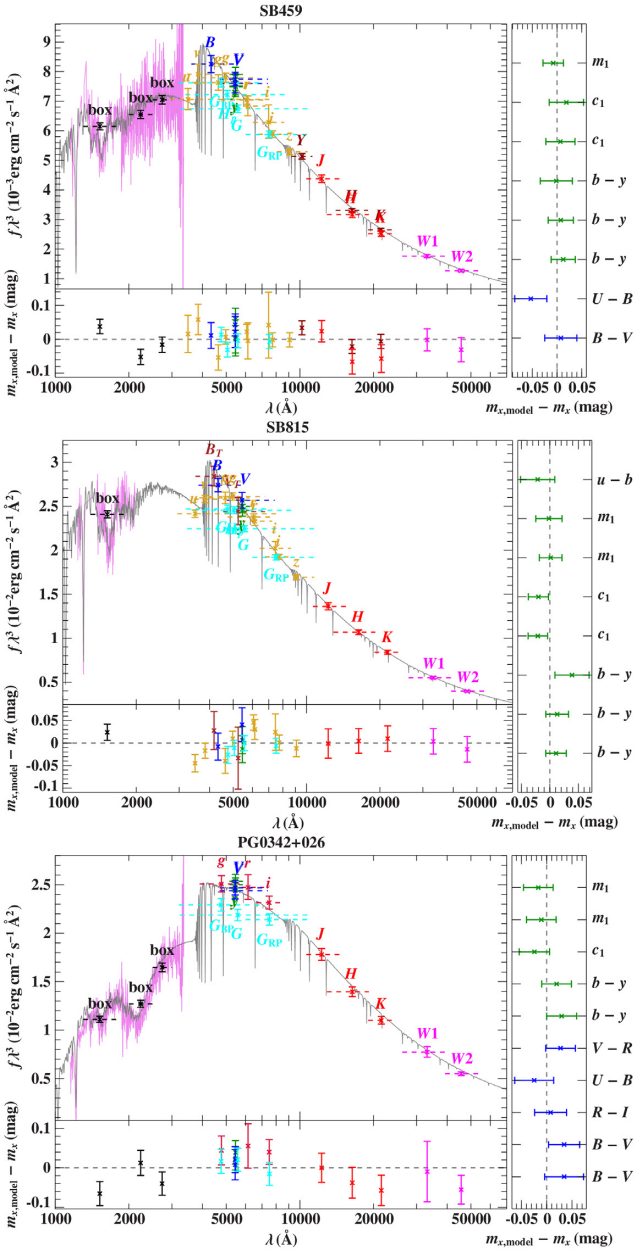

Figure 4. Matching the spectral energy distributions and colours of SB 459 (upper panel), SB 815 (middle panel), and PG0342 + 026 (lower panel). The coloured observed magnitudes (*IUE* box: black, SDSS: blue; SkyMapper: yellow; *Gaia*: cyan; VISTA: dark red; 2MASS: red, *WISE*: magenta) were derived from filter-averaged fluxes. The dashed horizontal lines indicate the filter widths. A model SED calculated with the spectroscopic parameters is overplotted as a solid grey line. Also overlayed are the *IUE* spectra in magenta. The panels below (SED) and to the right (colours) of the main panel show the residuals for the magnitudes and colours.

4 LIGHT VARIATIONS

All three targets have been observed during single *TESS* sectors, which are specifically listed in Table 1, and have been observed in the SC mode, lasting 120 s. We performed our analysis by

Table 2. SB 459: Angular diameters, interstellar reddening parameter, *Gaia* parallax, and stellar parameters.

Object: SB459	68 per cent confidence interval
Angular diameter log(Θ (rad))	-10.6134 ± 0.0016
Color excess $E(B-V)$	0.0049 ± 0.0021 mag
Parallax ϖ (*Gaia*, RUWE = 1.17)	2.37 ± 0.07 mas
Effective temperature $T_{\rm eff}$ (prescribed)	24900 ± 500 K
Surface gravity log(g (cm s^{-2})) (prescribed)	5.35 ± 0.10
Helium abundance log(n(He)) (fixed)	-2.58
Radius $R_\star$	0.228 ± 0.007 R$_\odot$
Mass $M_\star$	0.42 ± 0.11 M$_\odot$
Luminosity log $\left(\frac{L}{[L_\odot}\right)$	1.25 ± 0.05

Table 3. Same as Table 2, but for SB 815.

Object: SB815	68% confidence interval
Angular diameter log(Θ (rad))	$-10.3920^{+0.0018}_{-0.0017}$
Colour excess $E(B-V)$	$0.0018^{+0.0025}_{-0.0018}$ mag
Parallax ϖ (*Gaia*, RUWE = 1.23)	4.07 ± 0.10 mas
Effective temperature $T_{\rm eff}$ (prescribed)	27200 ± 550 K
Surface gravity log(g (cm s^{-2})) (prescribed)	5.39 ± 0.10
Helium abundance log(n(He)) (fixed)	-2.94
Radius $R_\star$	0.221 ± 0.005 R$_\odot$
Mass $M_\star$	0.44 ± 0.11 M$_\odot$
Luminosity log $\left(\frac{L}{[L_\odot}\right)$	1.38 ± 0.05

Table 4. Same as Table 2, but for PG0342 + 026.

Object: PG0342 + 026	68 per cent confidence interval
Angular diameter log(Θ (rad))	-10.2975 ± 0.0025
Color excess $E(B-V)$	0.128 ± 0.004 mag
Parallax ϖ (*Gaia*, RUWE = 1.28)	6.13 ± 0.13 mas
Effective temperature $T_{\rm eff}$ (prescribed)	26000 ± 1100 K
Surface gravity log(g (cm s^{-2})) (prescribed)	5.59 ± 0.12
Helium abundance log(n(He)) (fixed)	-2.69
Radius $R_\star$	0.182 ± 0.004 R$_\odot$
Mass $M_\star$	0.47 ± 0.14 M$_\odot$
Luminosity log $\left(\frac{L}{[L_\odot}\right)$	1.13 ± 0.08

using the corrected time series data extracted through the *TESS* data processing pipeline developed by NASA's Science Processing Operation Centre. These processed data are publicly available in the Mikulski Archive for Space Telescopes data base. We collected these files and have done further analysis. We extracted PDCSAP_FLUX, which is corrected for on-board systematics and neighbours' contribution to the overall flux. We clipped fluxes at 5σ to remove outliers, de-trended long-term variation (longer than days). Finally, we normalized fluxes by calculating $(fl/ < f > -1)*1000$, deriving *part per thousand* (ppt). We show the resultant light curves of each target in the top panels of Fig. 5.

4.1 Fourier analysis

We used a Fourier technique for identifying the frequency of pulsations. Since we have only about 27 d long SC data for each target, the frequency resolution is 0.64 μHz as defined by $1.5/T$, where T is the time coverage of the data (Baran 2012). The standard pre-whitening procedure has been used by fitting the peaks with $A_i \sin(2\pi f_i t + \phi_i)$ by means of a non-linear least-square method. We have used our custom pipeline for this purpose. We pre-whitened the data down to the detection threshold defined as 4.5 times the mean noise level, i.e. the signal-to-noise ratio, S/N = 4.5, calculated from the residual amplitude spectra. The threshold has been discussed by Baran, Koen & Pokrzywka (2015) and Zong et al. (2016), who reported slightly higher threshold than in case of ground-based data. The SC mode sampling translates to the Nyquist frequency of 4166 μHz. In case of SB 815 we found some frequencies in the p-mode range, close to the Nyquist frequency and, following a discovery of a reflection across Nyquist (Baran et al. 2012), we also searched the amplitude spectrum above the Nyquist frequency in order to see if any of subNyquist p modes have superNyquist origin. An amplitude and a profile of the peaks in the sub and superNyquist regions help identifying the origin of the signal. Since the Nyquist frequency is not fixed in time, the reflections will look smeared out and therefore lower in amplitude, however, this effect works best if the satellite motion covers substantial part of the orbit, which does not happen in case of single sector data. Therefore, we assume that all frequencies in the p-mode region originate in the subNyquist range are real, but this should be confirmed with shorter cadence data, presumably during the second phase of *TESS* mission, when 20 s cadence will be accessible.

In SB 459, we detected 22 frequencies above the detection threshold with 207.314 μHz being the highest amplitude one at 1.72 ppt, and all are in the g-mode region. In SB 815, we detected 37 frequencies in the g-mode region and six frequencies in the p-mode region, with the highest amplitude (1.642 ppt) frequency at 258.1878 μHz. In PG 0342 + 026, we detected 27 frequencies, with 219.274 μHz having the highest amplitude of 0.758 ppt. We list all frequencies detected in those three stars in Tables 5, 6, and 7.

SB 815 turned out to be a hybrid pulsator. The highest amplitude of 1.296 ppt in the p-mode region shows at 2582.8740 μHz. The signal at high frequencies is parted into two groups. The first one contains four frequencies, while the second one has two low-amplitude frequencies. We found the separation between these two groups to be around 896 μHz. Such spacing has been previously reported by Baran et al. (2009), who concluded that such groups may represent modes with two consecutive radial orders.

4.2 Multiplets

Multiplets are a result of stellar rotation that changes frequency of modes with the same modal degree and $m \neq 0$. The frequency change also depends on a rotation period of a star. For a given modal degree l there is $2l + 1$ components differing in an azimuthal order m, therefore by the number of components in an identified multiplet we can infer the modal degree.

We could not detect multiplets in any of these three targets. The reason for null detection may be not long enough data coverage, which causes the frequency resolution not to be high enough to resolve multiplet components. A common rotation period derived in sdB stars is around 40 d (e.g. Baran et al. 2012; Baran & Winans 2012; Telting et al. 2012; Østensen et al. 2014; Foster et al. 2015; Charpinet et al. 2018), which, in case of p modes, translates to 0.29μHz or half the frequency resolution of our data, though exceptions are found (Baran et al. 2009; Reed et al. 2014). Another explanation may be a pole-on orientation of a pulsation axis, however, we consider this explanation to be very unlikely, since we do not expect all three randomly chosen targets to be oriented in exactly the same way. In case the amplitudes of the side components

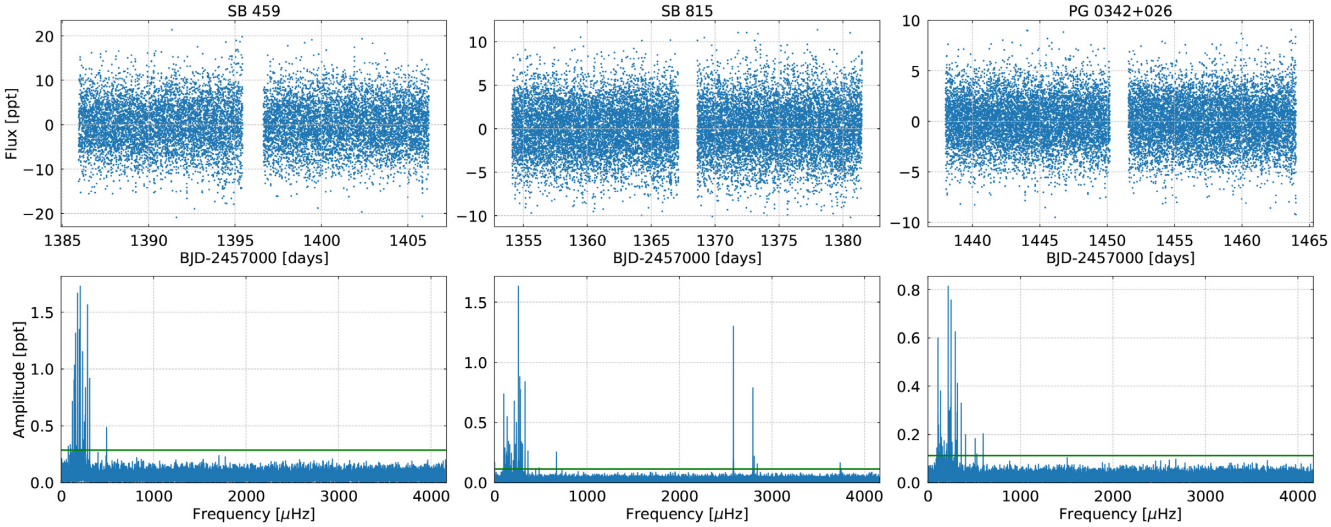

Figure 5. The upper panels show the light curves, while the bottom panels show the amplitude spectra. The green horizontal line in the bottom panels denotes 4.5σ threshold.

Table 5. List of frequencies detected in SB 459.

ID	Frequency (μHz)	Period (s)	Amplitude (ppt)	S/N	l	n
f_1	77.82(5)	12 849.8(9.0)	0.30(5)	4.5		
f_2	100.092(48)	9990.8(4.7)	0.34(5)	5.2	1	39
f_3	122.319(22)	8175.3(1.5)	0.74(5)	11.1	1/2	32/55
f_4	126.27(5)	7919.5(3.3)	0.31(5)	4.6	1	31
f_5	140.180(19)	7133.7(10)	0.86(5)	12.9	1	28
f_6	145.213(17)	6886.4(8)	0.97(5)	14.6	1	27
f_7	156.802(13)	6377.5(5)	1.30(5)	19.6	1/2	25/43
f_8	163.519(48)	6115.5(1.8)	0.34(5)	5.1	1	24
f_9	178.170(10)	5612.63(31)	1.66(5)	24.9	1	22
f_{10}	196.322(12)	5093.67(31)	1.36(5)	20.4	1	20
f_{11}	207.314(9)	4823.61(22)	1.72(5)	25.8	1	19
f_{12}	221.87(5)	4507.2(1.1)	0.30(5)	4.6		
f_{13}	233.175(14)	4288.63(26)	1.17(5)	17.6	1	17
f_{14}	234.566(42)	4263.2(8)	0.39(5)	5.9		
f_{15}	242.460(42)	4124.4(7)	0.39(5)	5.9	2	28
f_{16}	246.917(46)	4049.9(8)	0.35(5)	5.3	1	16
f_{17}	251.341(32)	3978.7(5)	0.51(5)	7.7	2	27
f_{18}	261.184(28)	3828.72(40)	0.60(5)	9.0	2	26
f_{19}	263.905(20)	3789.24(28)	0.84(5)	12.6	1	15
f_{20}	286.201(10)	3494.05(13)	1.58(5)	23.7	1	14
f_{21}	309.779(17)	3228.11(18)	0.93(5)	14.0	1/2	13/22
f_{22}	492.395(34)	2030.89(14)	0.47(5)	7.1	2	14

are low, below the detection threshold, these components will not be detected, either.

4.3 Asymptotic period spacing

Another method that helps identifying modes relies on periods and not frequencies. In the asymptotic limit, *i.e.* $n \gg l$, consecutive overtones of g modes are nearly equally spaced in period (e.g. Charpinet et al. 2000; Reed et al. 2011). The pulsation period of a given mode with degree l and radial order n can be expressed as

$$P_{l,n} = \frac{P_0}{\sqrt{l(l+1)}} n + \epsilon \qquad (1)$$

where P_0 is the period of the fundamental radial mode and ϵ is an offset (Unno et al. 1979). Thus, for two consecutive radial overtones and a given modal degree, a difference (commonly called as *period spacing*) of their periods should be constant, dependent of the modal degree and independent of the radial order.

$$\Delta P_l = P_{l,n+1} - P_{l,n} = \frac{P_0}{\sqrt{l(l+1)}}. \qquad (2)$$

Using equation (1) it is possible to assign the radial order n to the precision of some arbitrarily chosen offset n_l. We provide those values in Tables 5, 6, and 7. Using equation (2) we can also derive a ratio between a period spacing of modes of different modal degree, e.g. the ratio between dipole and quadrupole modes equals $1/\sqrt{3}$. This is very strong constraint, since having the period spacing for dipole modes, we can estimate the expected value for higher degree modes. Previous analyses of photometric space data of sdBVs show that the average period spacing of dipole modes is nearly 250 s on average (Reed et al. 2018a). The average spacing for quadrupole modes is found to be close to the expected value, being a result of the ratio given above.

Best, if the mode identification is done based on both features, multiplets, and period spacing, since they complement each other providing more convincing conclusion on a mode assignment, very often helping to start finding a specific modal degree sequence. In our case, we had to rely solely on the period spacing. We started our modal degree assignment with the highest amplitude modes. This assumption is justified by the surface cancellation effect, which causes that modes with higher degrees have smaller observational amplitudes. In this consideration, it is assumed that all modes have the same intrinsic amplitudes, which may not necessarily be correct, however, our thus far experience clearly shows that most of the high-amplitude frequencies in sdBV stars are dipole modes. Despite of this assumption, if two peaks satisfy both dipole and quadrupole sequences, we mentioned both values in tables and figures. In échelle and reduced period diagrams we have added these points with different colour coding. The average period spacing in sdBVs detected thus far is between 200 and 300 s. To guess the average spacing in our targets, we calculated the *Kolmogorov–Smirnov* (KS) test and we plotted the results in Fig. 6. The meaning of a Q value and more details on this test is provided by Kawaler (1988). Basically,

Table 6. List of frequencies detected in SB 815.

ID	Frequency (μHz)	Period (s)	Amplitude (ppt)	S/N	l	n
f_1	100.438(7)	9956.4(7)	0.718(21)	27.3	1	38
f_2	103.574(39)	9655.0(3.6)	0.125(21)	4.8	1	37
f_3	106.159(34)	9419.8(3.0)	0.141(21)	5.4	1/2	36/62
f_4	112.435(31)	8894.0(2.4)	0.228(22)	8.7		
f_5	112.789(24)	8866.1(1.9)	0.291(22)	11.1	1	34
f_6	123.734(32)	8081.9(2.1)	0.149(21)	5.7	1	31
f_7	128.523(22)	7780.7(1.3)	0.217(21)	8.3	1	30/t
f_8	131.737(20)	7590.9(1.2)	0.242(21)	9.2	1/2	29/50
f_9	136.885(9)	7305.4(5)	0.534(22)	20.3	1	28
f_{10}	137.674(27)	7263.5(1.4)	0.186(22)	7.1	2	48
f_{11}	142.334(26)	7025.7(1.3)	0.193(22)	7.3	1	27
f_{12}	142.858(26)	6999.9(1.3)	0.189(22)	7.2		
f_{13}	151.999(14)	6579.0(6)	0.345(21)	13.1	1	25/t
f_{14}	154.178(37)	6486.0(1.5)	0.132(21)	5.0		
f_{15}	165.197(16)	6053.4(6)	0.306(21)	11.6	2	40
f_{16}	174.841(36)	5719.5(1.2)	0.133(21)	5.1	1	22
f_{17}	182.576(20)	5477.2(6)	0.238(21)	9.0	1	21
f_{18}	202.345(27)	4942.1(7)	0.179(21)	6.8	1	19
f_{19}	213.908(7)	4674.92(16)	0.671(21)	25.6	1/2	18/31
f_{20}	226.812(15)	4408.93(29)	0.328(21)	12.5	1	17
f_{21}	228.836(39)	4369.9(7)	0.123(21)	4.7	2	29
f_{22}	236.890(10)	4221.36(17)	0.489(21)	18.6	2	28
f_{23}	246.268(38)	4060.6(6)	0.125(21)	4.8	2	27
f_{24}	258.1879(29)	3873.149(44)	1.642(21)	62.5	1	15
f_{25}	266.359(24)	3754.33(33)	0.204(21)	7.8	2	25
f_{26}	273.537(5)	3655.82(7)	0.878(21)	33.4	1	t
f_{27}	277.625(34)	3601.99(44)	0.143(21)	5.4	2	24
f_{28}	279.723(6)	3574.96(8)	0.777(21)	29.6	1	14
f_{29}	285.303(34)	3505.05(42)	0.141(21)	5.4		
f_{30}	289.809(14)	3450.55(16)	0.353(21)	13.4	2	23
f_{31}	302.183(37)	3309.26(40)	0.137(22)	5.2		
f_{32}	302.892(14)	3301.51(16)	0.353(22)	13.4	1/2	13/22
f_{33}	330.565(6)	3025.12(5)	0.848(21)	32.3	1	12
f_{34}	361.604(19)	2765.46(14)	0.257(21)	9.8	1	11
f_{35}	445.775(40)	2243.29(20)	0.121(21)	4.6	1	9
f_{36}	482.523(40)	2072.44(17)	0.119(21)	4.5	2	14
f_{37}	669.836(19)	1492.902(42)	0.255(21)	9.7		
f_{38}	2582.8740(37)	387.1656(6)	1.296(21)	49.3		
f_{39}	2793.905(6)	357.9219(8)	0.786(21)	29.9		
f_{40}	2808.165(22)	356.1045(28)	0.214(21)	8.1		
f_{41}	2841.082(31)	351.9786(39)	0.153(21)	5.8		
f_{42}	3737.134(28)	267.5848(20)	0.169(21)	6.4		
f_{43}	3747.579(40)	266.8390(29)	0.118(21)	4.5		

this test provides the most common values of period spacings that exist in the data. The result of our mode identification based on the asymptotic period spacing is also presented in échelle diagrams, which we discuss in Section 4.4.

4.3.1 SB 459

The KS test shows a common spacing of periods around 260 s shown in the left-hand panel of Fig. 6. We identified 12 dipole modes, four quadrupole modes, and three peaks satisfying both sequences. We marked them in the amplitude spectrum in Fig. 7. Linear fits provide the average period spacings of 259.16(56) s and 149.89(5) s for dipole and quadrupole modes, respectively.

Table 7. List of frequencies detected in PG 0342 + 026.

ID	Frequency (μHz)	Period (s)	Amplitude (ppt)	S/N	l	n
f_1	96.786(35)	10332.1(3.7)	0.145(21)	5.5		
f_2	108.889(9)	9183.7(7)	0.593(21)	22.6	1/2	40/69
f_3	114.621(23)	8724.4(1.7)	0.222(21)	8.5	1	38
f_4	124.720(42)	8018.0(2.7)	0.120(21)	4.6	1	35
f_5	128.559(32)	7778.5(1.9)	0.161(21)	6.1	1	34
f_6	132.313(32)	7557.8(1.8)	0.160(21)	6.1	1	33
f_7	136.448(13)	7328.8(7)	0.391(21)	14.9	1	32
f_8	145.763(28)	6860.5(1.3)	0.185(21)	7.0	1	30
f_9	150.803(39)	6631.2(1.7)	0.131(21)	5.0	1	29
f_{10}	156.352(34)	6395.8(1.4)	0.152(21)	5.8	1	28
f_{11}	175.286(30)	5705.0(10)	0.170(21)	6.5	1/2	25/43
f_{12}	198.546(36)	5036.6(9)	0.141(21)	5.4	2	38
f_{13}	204.375(30)	4893.0(7)	0.167(21)	6.3	2	37
f_{14}	219.274(6)	4560.50(13)	0.819(21)	31.1	1	20
f_{15}	231.527(17)	4319.16(32)	0.298(21)	11.3	1	19
f_{16}	243.921(17)	4099.69(28)	0.307(21)	11.7	1/2	18/31
f_{17}	250.256(7)	3995.90(11)	0.758(21)	28.8	1	t
f_{18}	260.620(30)	3837.00(45)	0.167(21)	6.4	1/2	17/29
f_{19}	295.891(8)	3379.62(9)	0.623(21)	23.7	1	15
f_{20}	303.246(28)	3297.65(30)	0.181(21)	6.9	2	25
f_{21}	315.536(20)	3169.21(20)	0.252(21)	9.6	2	24
f_{22}	318.907(13)	3135.71(13)	0.390(21)	14.8	1	14
f_{23}	359.953(15)	2778.14(12)	0.329(21)	12.5	1	t
f_{24}	406.920(26)	2457.48(16)	0.194(21)	7.4	1	11
f_{25}	510.726(28)	1958.00(11)	0.182(21)	6.9	1/2	9/15
f_{26}	529.408(43)	1888.90(15)	0.119(21)	4.5		
f_{27}	597.478(25)	1673.70(7)	0.204(21)	7.8		

4.3.2 SB 815

In our analysis, we detected six frequencies in the p-mode region and we excluded those from our KS test, which eventually points at a common spacing of around 264 s (middle panel in Fig. 6). We arrived at two possible solutions that we present in Figs 8 and 9.

4.3.2.1 Solution 1 In this solution, we identified 17 dipole modes, nine quadrupole modes, while four peaks fit both sequences. Linear fits provide the average period spacings of 265.04(73) s and 153.02(11) s for dipole and quadrupole modes, respectively. We identified a frequency 273.537 μHz with an amplitude of 33.4σ, where σ denotes an average noise level, which fits neither dipole nor quadrupole sequence. Its amplitude is also much higher to consider it to be any $l \geq 3$ mode due to the surface cancellation effect (Dziembowski 1977). Therefore, we assigned it as a trapped dipole mode. This mode identification looks fairly good, but two frequencies 128.523 and 151.999 μHz differ excessively from the mean period spacing (28.5 per cent and 15.6 per cent, respectively). To justify these extreme deviations we followed the theoretical consideration provided by Charpinet et al. (2013) in fig. 4, which presents that thin hydrogen envelope sdBVs show higher deviations from the mean period spacing.

4.3.2.2 Solution 2 This solution considers those two extremely deviated frequencies as candidate for trapped modes. These peaks have moderate amplitudes (8.3σ and 13.1σ, respectively) and they do not fit the quadrupole sequence any better. Therefore, taking these two as trapped modes sorts out large deviations in the period sequence of the dipole modes. In this solution, we are left with 15 dipole modes with average period spacing of 265.15(57) s and three trapped modes.

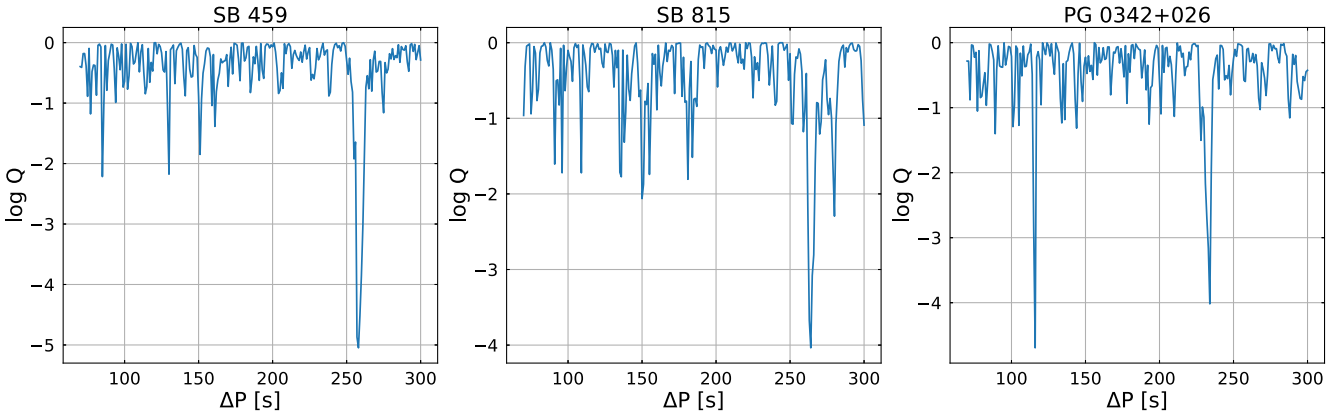

Figure 6. KS test for SB 459, SB 815 and PG 0342 + 026.

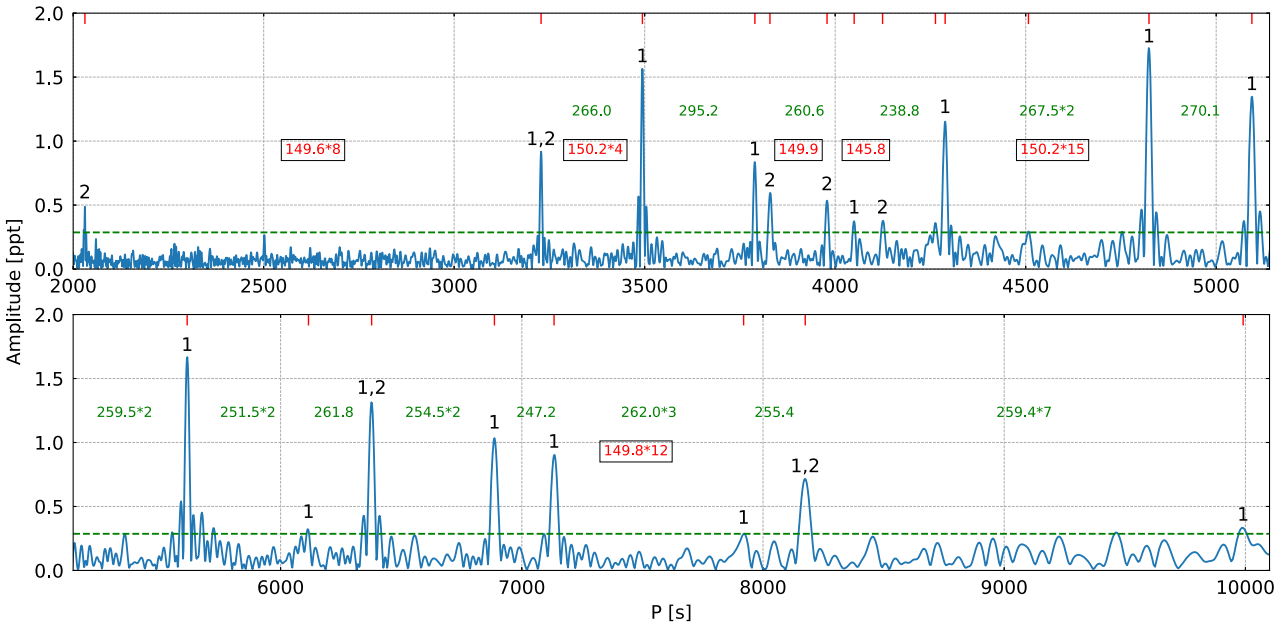

Figure 7. A close-up of the amplitude spectrum of SB 459 plotted in period instead of frequency. The green horizontal dashed line denotes the 4.5σ detection threshold. The values of modal degrees are shown on top of each identified modes. The values between frequencies denote period spacing between two overtones of the same degree (green for dipole and boxed red for quadrupole modes).

4.3.3 PG 0342 + 026

The KS test points at a common spacing around 232 s (right-hand panel in Fig. 6). There is another minimum of a log Q value at 116 s. It is close to the expected value of a period spacing of quadrupole modes (132 s), however, it is half the period spacing of dipole modes, which sometimes appears in this test. We identified 13 dipole modes, four quadrupole modes, and five modes satisfying both sequences. We marked all identified modes in the amplitude spectrum in Fig. 10. A linear fit provides the average period spacings 232.25(30) and 133.74(10) s for dipole and quadrupole modes, respectively. Two frequencies seem to be candidates for trapped modes and we refer to Section 4.4 for more details.

We have collected average period spacings (ΔP) as a function of effective temperature for sdBV stars from the literature. All these collected information for 27 sdBVs is provided in Table 8. We plotted these two parameters in Fig. 11. We stress that the sample is not very large yet and any conclusion maybe biased. The first try of finding correlation between ΔP and $T_{\rm eff}$ has been undertaken by Reed et al. (2011) with null result. We increased the number of points but our plot shows that still no clear correlation is present. There are zones of avoidance, though they may just be lacking data points as a consequence of a small sample. Therefore, based on our findings, we conclude that the average period spacing does not correlate with $T_{\rm eff}$ and so ΔP does not translate to a specific $T_{\rm eff}$ and vice versa.

4.4 Échelle diagrams and candidates for trapped modes

The échelle diagrams are very useful tools for testing the identification of the modes by means of the asymptotic period spacing. These diagrams represent $P\,mod\ \Delta P$ in function of P, where P is the pulsation period and ΔP is a period spacing. We present the diagrams for all three targets in Fig. 9. For SB 815 we include two solutions. The upper panels show the échelle diagrams for dipole modes while the bottom panels show the diagrams for quadrupole modes. Peaks satisfying both the sequences have been added to both

Table 8. Effective temperature and average period spacing data for known sdBVs. The first reference is for ΔP and the second is for $T_{\rm eff}$. References: 1. Reed et al. (2018a), 2. Silvotti et al. (2019), 3. Reed et al. (2011), 4. Holdsworth et al. (2017), 5. Sanjayan et al. (in preparation), 6. Charpinet et al. (2019), 7. Reed et al. (2020).

Name	ΔP (s)	$T_{\rm eff}$ (kK)	References
KIC 1718290	276(1)	21.8(1)	1,4
KIC 2437937	234.73(52)	24.7(6)	5,4
KIC 2438324	235.49(51)	26.2(4)	5,4
KIC 2569576	244.31(46)	24.5(4)	5,4
KIC 2697388	240.06(19)	23.9(3)	1,4
KIC 2991403	268.52(74)	27.3(2)	1,4
KIC 3527751	266.4(2)	27.9(1)	1,4
KIC 5807616	242.12(62)	27.3(2)	1,4
KIC 7664467	260.02(77)	26.8(5)	1,4
KIC 7668647	247.8	27.7(3)	1,4
KIC 8302197	258.61(62)	27.2(2)	1,4
KIC 9472174	255.63(30)	29.6(1)	1,4
KIC 10001893	268.0(5)	26.7(3)	1,4
KIC 10553698	263.15	27.5(2)	1,4
KIC 10670103	251.6(2)	21.1(3)	1,4
KIC 11179657	231.02(2)	26.0(8)	1,4
KIC 11558725	244.45(32)	27.7(1)	1,4
EPIC 201206621	268(1)	27.954(54)	1,4
EPIC 202065500	234	29.85	1,4
EPIC 203948264	261.34(78)	26.76(61)	1,4
EPIC 211696659	227.05(56)	27.12(64)	1,4
EPIC 211779126	253.3(8)	28.542(82)	1,4
EPIC 212707862	252.6(1.1)	28.298(162)	1,4
EPIC 218366972	251	28.2	1,4
EPIC 218717602	260	24.85	1,4
EPIC 220641886	256.5(1)	23.47(65)	2,2
KPD 0629−0016	247.17(48)	27.4(3)	3,4
TIC 013145616	268.85(32)	29.60(38)	7,7
TIC 278659026	245.71(75)	23.72(26)	6,6

dipole and quadrupole échelle diagrams and represented with green colour points. The right vertical axes show the radial orders with respect to an offset n_l from the real radial k order. The k number can only be determined from modelling (e.g. Charpinet et al. 2000).

The asymptotic relation, defined by equation 2, is strict only for homogeneous stars. In that case, standing waves of g-modes oscillate in a cavity created e.g. by the convective zone and the surface of a star. Then, the consecutive overtones are spaced equally in period and in an échelle diagram we can see a vertical ridge for a given modal degree. However, in a real star, as the density is not uniform, the ridge almost never becomes purely vertical. Some jitter appears. Since this feature is a consequence of a non-uniform structure of a star, deviations from a vertical ridge bear information about a chemical profile and hence cavities. Baran & Winans (2012) reported on a deviation from the vertical ridge, being a common property of many sdB stars (Baran et al. 2019). The so-called a 'hook' feature has never been explained thus far but surely must be accounted for if reliable models are to be calculated.

In a few cases, frequencies did not fit well either sequence. The reason may be hidden deep in the sdB interior where the H/He or C/He transition layers between the convective core and the surface appear. These boundaries may contribute to create additional cavities causing some modes to be imprisoned in smaller cavities. Those modes are called trapped modes and they do not follow an asymptotic sequence. The theoretical explanation was provided by Charpinet et al. (2000) and Ghasemi et al. (2017).

There is a 'hook' feature in SB 459 between 3000 and 7000 s, while in PG 0342 + 026 the feature is not as pronounced. The largest jitter appears in SB 815 which deviates from the mean period spacing by 28.5 per cent. The upper part of the ridge is not smooth, winding from side to side. That is why we decided to present two solutions for this target. In the absence of multiplets, it is always difficult to make sure that a mode identification is fully correct. Our first solution contains the largest jitter but it provides the 'hook' feature in between 3000 and 7000 s. In our second solution, we removed two extremely deviated points (6579.0 s and 7780.7 s) from the dipole mode sequence, and marked them as trapped mode candidates. In the latter solution the échelle diagram looks more smooth and still shows the 'hook' feature. With no multiplets detected our identification will always suffer from doubts in modal degree assignment, mostly because period spacing sequences of different modal degree cross each other and some of the modes are fitting both sequences fairly well. In case of high-amplitude frequencies we prefer $l = 1$ rather than higher degrees. The ridges of quadrupole modes are fairly short and those modes are mostly leftovers from $l = 1$ assignment.

One of the best tools to look for trapped modes is a reduced period diagram. The diagram presents a reduced period $\Pi = P \cdot \sqrt{l(l+1)}$ in function of a reduced period spacing $\Delta\Pi = \Delta P \cdot \sqrt{l(l+1)}$. This multiplication causes sequences of all modal degrees to overlap. Overall, the shape of the plot would be similar to what we see in the échelle diagrams, though it will be twisted, so the ridge is now horizontal. Modes with different modal degrees overlap, however, what is more important, the candidates for trapped modes of different degrees also overlap. It can be clearly seen in the papers by e.g. Østensen et al. (2014), Uzundag et al. (2017), and Baran et al. (2017). The actual periods of those trapped modes differ between modal degrees, so it is not easy to spot them in amplitude spectra, however, the multiplicative factor brings them all in one place in this diagram.

We show the reduce period diagrams for two targets, SB 815 (two solutions) and PG 0342 + 026 in Fig. 12. In SB 459, the sequence of quadrupole modes is too short, not pointing at any trapped mode candidates, which makes the diagram completely inconclusive, and that is why we decided not to present it. In the first solution of SB 815 and in PG 0342+026, the candidates for trapped modes appear to be at the shortest periods. It looks similar to the diagrams reported by the other authors mentioned above. In SB 815 we find either one (solution 1) or three (solution 2), while in PG 0342+026 we find two candidates for trapped modes. Two longest periods trapped modes in SB 815 (solution 2) and two trapped modes in PG 0342 + 026 are separated by almost 2 000 s. It agrees with values reported by the other authors and calculated from theoretical considerations reported by Charpinet et al. (2000). Unluckily, in PG 0342 + 026 the quadrupole sequence does not extend to overlap with those candidates and therefore we cannot confirm trapped mode identification. Likewise in SB 815 (solution 1). In the case of solution 2, although the dipole and quadrupole sequences overlap, we detected no quadrupole trapped modes candidates. This makes those dipole trapped modes candidates less reliable. They can still serve as an additional constraint in modelling, help deriving the most reliable solution and understand the chemical profile inside sdB stars, which is responsible for trapped modes.

5 EVOLUTIONARY STATUS

The stellar atmospheric parameters such as effective temperature $T_{\rm eff}$ and surface gravity $\log g/({\rm cm\,s^{-2}})$ have great importance to

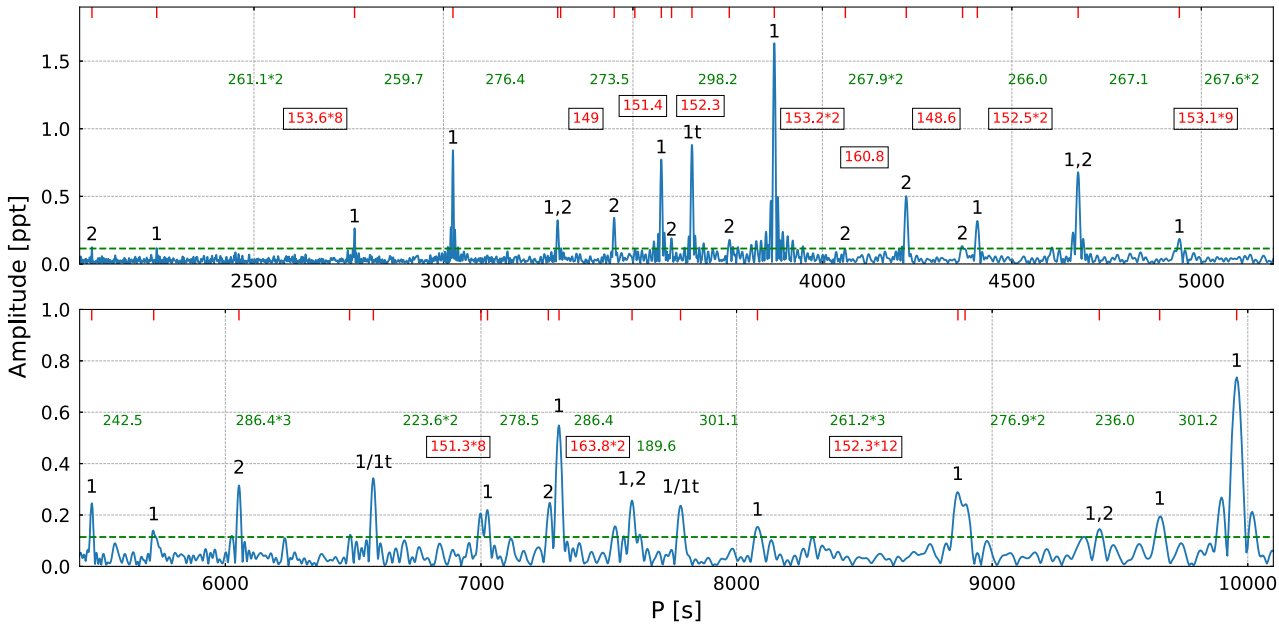

Figure 8. Same as Fig. 7 but for SB 815.

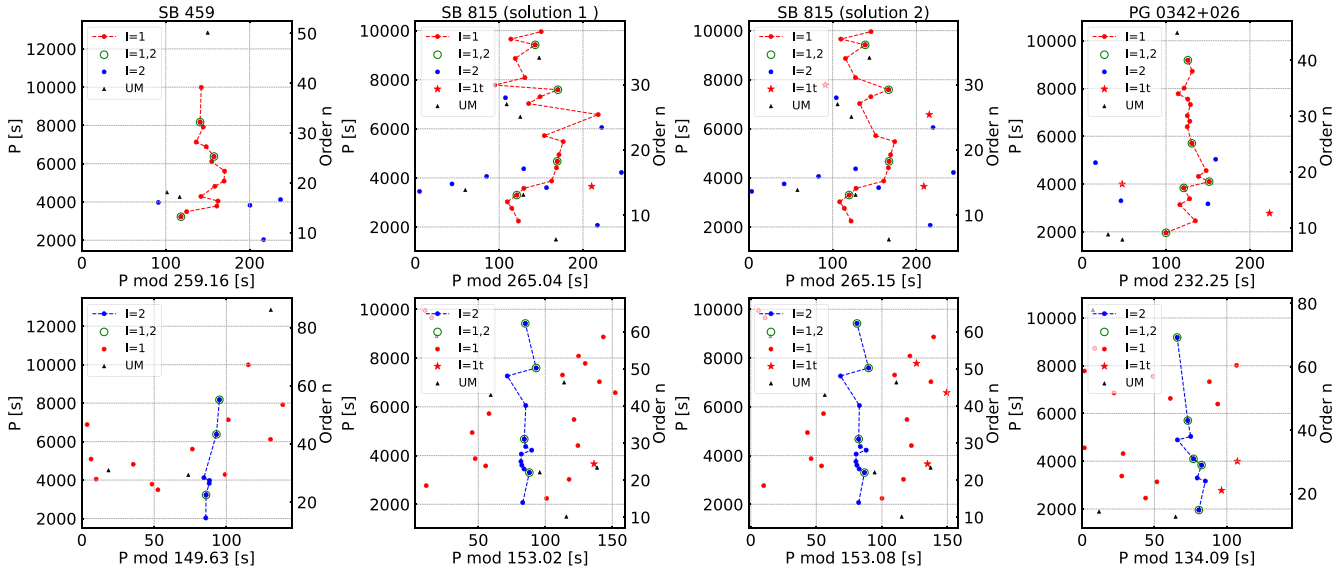

Figure 9. Échelle diagrams for dipole (top panels) and quadrupole (bottom panels) modes. In legends, '$l = 1t$' denotes dipole trapped modes and 'UM' denotes undefined modes.

determine physical conditions of stellar atmospheres. We have taken these two spectroscopic parameters of all sdBVs known to date from Holdsworth et al. (2017) and for our three *TESS* targets from Table 1. We have plotted these three targets along with 118 other previously known sdBVs in the effective temperature – surface gravity diagram (Fig. 13). In the plot, we can distinguish three different regions i.e. low $T_{\rm eff}$ and $\log g/(\mathrm{cm\,s^{-2}})$ containing g-mode pulsators (shown in cyan squares), high $T_{\rm eff}$ and $\log g/(\mathrm{cm\,s^{-2}})$ containing p-mode pulsators (shown in black circles), and the hybrid pulsators region (shown in magenta triangles) containing pulsators that show both p and g modes. Three *TESS* targets have been shown with bigger symbols along with the error bars. SB 459 and PG 0342 + 026 are located among g-mode pulsators, which is consistent with the frequency content of these two stars. The amplitude spectrum of SB 815 contains both g mode and p mode, which is also confirmed by its location in the plot.

In Fig. 13, we also plotted theoretical evolutionary tracks to assess the evolutionary status of our three targets. The tracks have been calculated using publicly available open source code MESA (Modules for Experiments in Stellar Astrophysics; Paxton et al. 2011, 2013, 2015, 2018, 2019), version 11701. We started with a pre-main-sequence model of a solar mass star, assumed a proto-solar chemical composition of Asplund et al. (2009) ($Z = 0.142$, $Y = 0.2703$), and evolved the model to the tip of the red giant branch. Then, before the helium flash, we removed most of its mass leaving only a residual hydrogen envelope on top of the helium core. The model was then relaxed to an equilibrium state and evolved until the depletion of helium in the core. All physical and

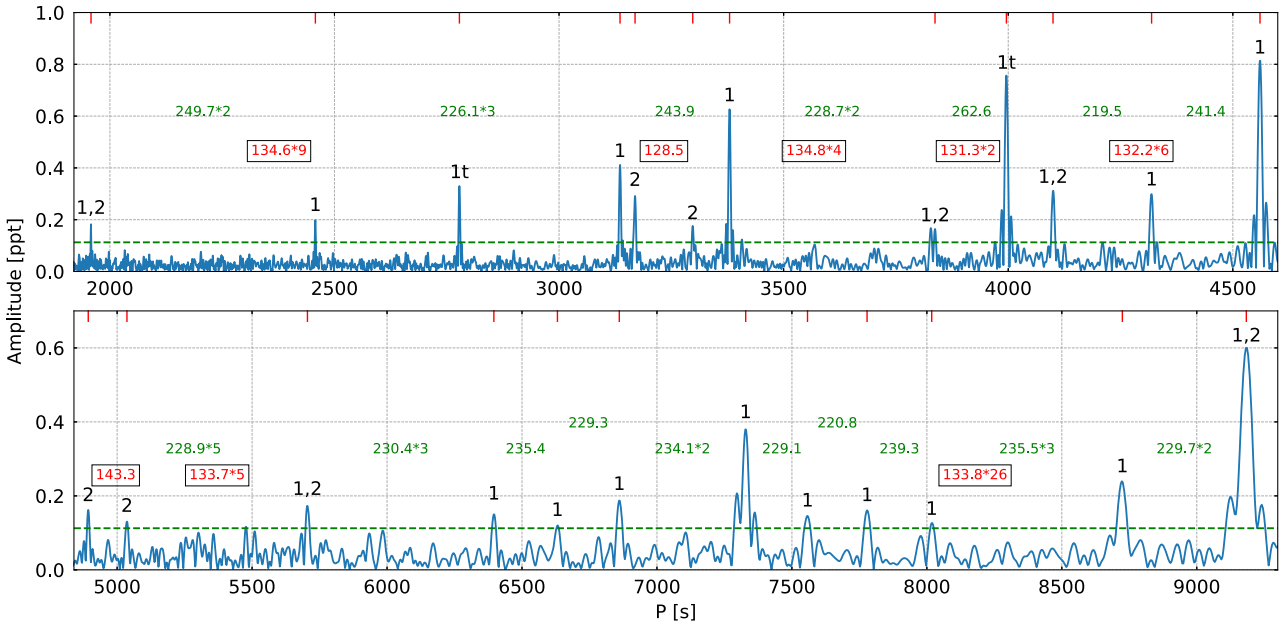

Figure 10. Same as Fig. 7 but for PG 0342 + 026.

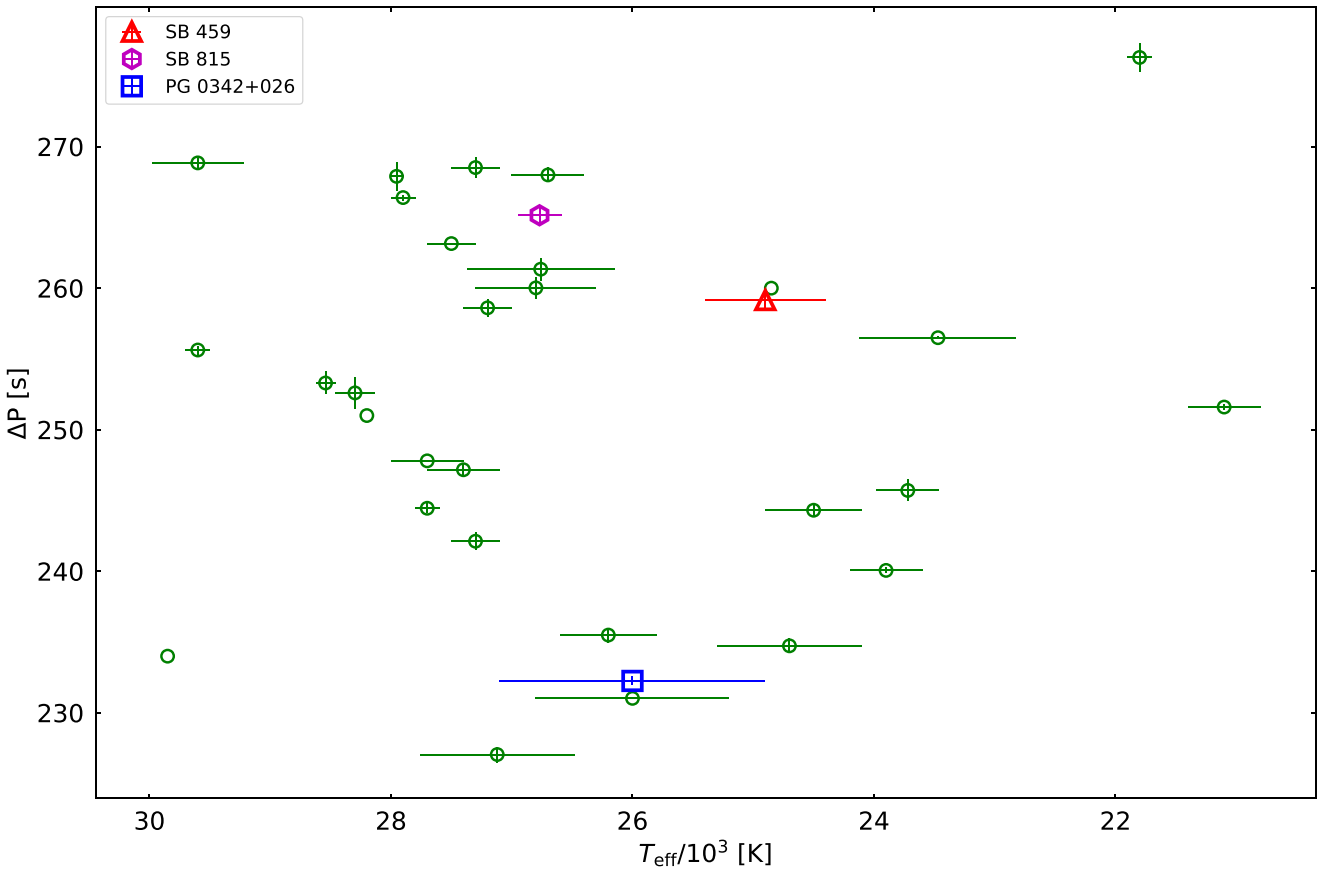

Figure 11. Effective temperature in function of an average period spacing.

numerical details of the models are discussed in Ostrowski et al. (in preparation). The models use predictive mixing to ensure proper growth of the convective core during the course of evolution (Paxton et al. 2018). The evolutionary tracks presented in Fig. 13 show stable core He burning phase of the sdB evolution. Different tracks correspond to models with different hydrogen envelope masses ($M_{\rm env} = 6 \times 10^{-4} - 5 \times 10^{-3}\,{\rm M}_{\odot}$). It may be noted that the effect

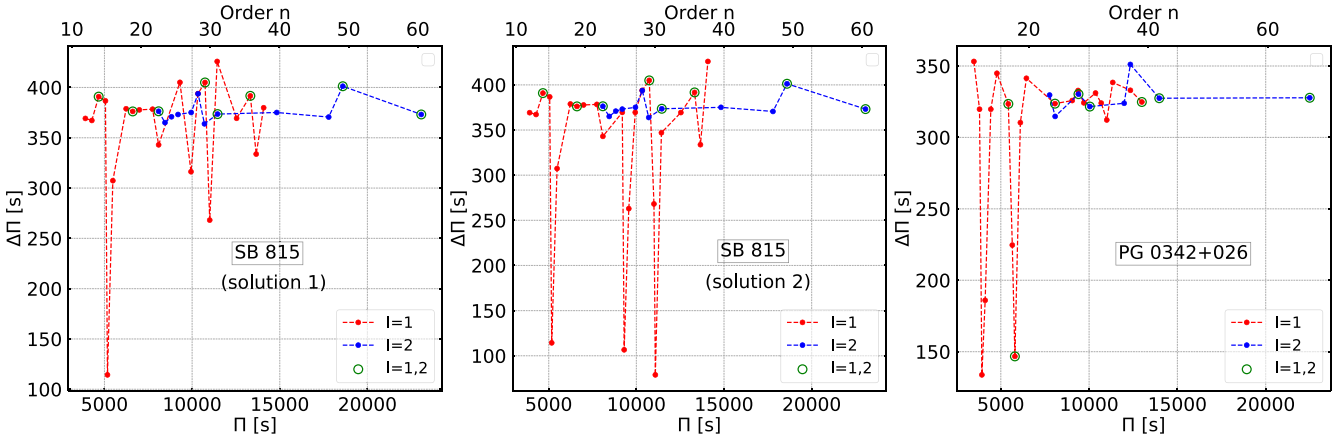

Figure 12. Reduced period diagrams for SB 815 and PG 0342 + 026. See text for more details.

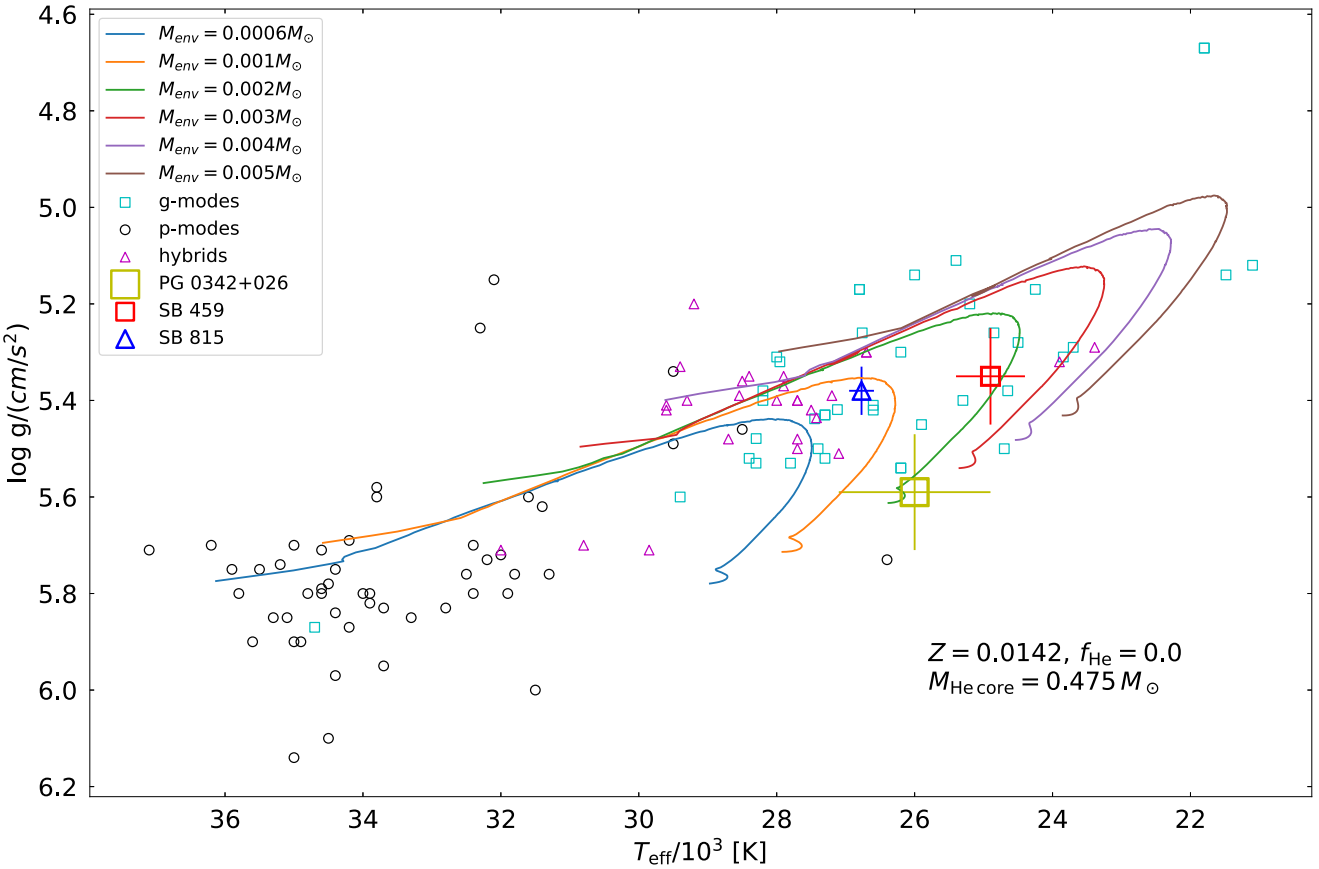

Figure 13. Evolutionary tracks of sdB stars in the log $g - T_{\rm eff}$ diagram for sdB stars with initial mass of $M_{\rm i} = 1.0\,{\rm M}_\odot$, mass of helium core $M_{\rm He,\,core} = 0.475\,{\rm M}_\odot$, and envelope masses of 6×10^{-4}–$5 \times 10^{-3}\,{\rm M}_\odot$. Observational data are taken from Holdsworth et al. (2017) along with three sdBVs explained in this paper.

of increasingly more massive hydrogen envelopes is to shift the evolutionary tracks towards lower effective temperatures.

The sdBs start their evolution toward lower effective temperatures and lower surface gravities. The direction of the evolution is reversed when the central helium abundance drops below about 10 per cent. The presented tracks fit the location of all our three targets very well and firmly confirm the three stars to be sdBs. All three targets are located on the He-core burning tracks. SB 459 fits really well to a track with an envelope mass of $M_{\rm env} = 2 \times 10^{-3}\,{\rm M}_\odot$ and still has more than half of its initial helium abundance available in the core. SB 815 is more advanced in its evolution with a central helium abundance of about 10 per cent and it is better fitted by a track with an envelope mass of $M_{\rm env} = 1 \times 10^{-3}\,{\rm M}_\odot$. The spectroscopic parameters of the star are determined with better precision than those of other two targets. PG 0342 + 026 seems to be the youngest sdBVs among the three stars, at the beginning of the sdB phase. The envelope mass of the star may vary between $M_{\rm env} = 1$–$3 \times 10^{-3}\,{\rm M}_\odot$.

6 SUMMARY

In this paper, we report our asteroseismic analysis of three sdBV stars observed by the *TESS* satellite. We have analysed amplitude spectra to detect pulsation modes and we used the asymptotic period spacing to describe modes' geometries. For SB 459 we found 12 dipole modes, four quadrupole modes, and three modes that can be assigned with either modal degree. For SB 815 we did not find a unique solution. In solution 1 we identified 17 dipole modes, nine quadrupole modes, and four modes that can be assigned with either modal degree. In solution 2, we identified the same number of modes, however two dipole modes are considered candidates for trapped modes. In PG 0342 + 026 we identified 13 dipole modes, four quadrupole modes, and five modes that can be assigned with either modal degree. We found none multiplets and therefore our mode identification should be taken with caution.

The average period spacings of dipole modes is around 259, 265, and 232 s for SB 459, SB 815, and PG 0342 + 026, respectively. In all three targets we detected only few quadrupole modes and hence average period spacing values for quadrupole modes calculated from the linear fits are not too precise. We used a theoretical relation between period spacings of dipole and quadrupole modes, instead.

We also found a few candidates for trapped modes, one/three in SB 815 and two in PG 0342 + 026. In the reduced period diagrams the trapped mode candidates are spaced by around 2000 s. This spacing is predicted by theoretical calculations and makes our conclusion more reliable, yet not absolutely convincing, since we detected no quadrupole trapped modes counterparts.

By making use of the high precision *Gaia* parallaxes and spectral energy distributions from the ultraviolet to the infrared spectral range we derived the fundamental stellar parameters mass, radius, and luminosity from spectroscopically determined effective temperatures and gravities. The results are consistent with the predictions of canonical stellar evolutionary models (Dorman et al. 1993), however, with large uncertainties on stellar mass due to large uncertainties on $\log g$.

The location of our three sdBVs in the effective temperature – surface gravity diagram confirms that SB 459 and PG 0342+026 are g-mode dominated sdBVs and SB 815 is g-mode dominated hybrid pulsator. Theoretical evolutionary tracks provide a coarse-grained approximation of physical properties of these stars like He-core and hydrogen envelope masses, sizes of their cores along with their evolutionary sdB stages. These tracks show that all three stars are during core-helium-burning phase, where SB 815 is much more evolved than other two and PG 0342 + 026 has just entered the sdB phase.

We also tried to look for any correlation between ΔP and $T_{\rm eff}$ with all previously known g-mode sdBVs along with our three *TESS* targets. We found no correlations though. We suspect to see some correlations with increasing data points. The asteroseismic analysis of these targets will help to constrain models for these stars. This paper is our first attempt to list g-mode rich sdBVs observed in *TESS* and to do mode identifications for these targets.

ACKNOWLEDGEMENTS

Financial support from the Polish National Science Center under projects No. UMO-2017/26/E/ST9/00703 and UMO-2017/25/B ST9/02218 is acknowledged. RR, UH, and AI gratefully acknowledge financial support by the Deutsche Forschungsgemeinschaft through grants HE1356,71-1 and IR190/1-1. Theoretical calculations have been carried out using resources provided by Wroclaw Centre for Networking and Supercomputing (http://wcss.pl), grant No. 265. Based on observations obtained at the European Organisation for Astronomical Research in the Southern Hemisphere under ESO observing program 0103.D-0511. Based on observations obtained at Las Campanas Observatory under the run code 0KJ21U8U. MU acknowledges financial support from CONICYT Doctorado Nacional in the form of grant number No: 21190886. RR has received funding from the postdoctoral fellowship programme Beatriu de Pinós, funded by the Secretary of Universities and Research (Government of Catalonia) and by the Horizon 2020 programme of research and innovation of the European Union under the Maria Skłodowska-Curie grant agreement No. 801370. KJB is supported by the National Science Foundation under Award No. AST-1903828. WZ acknowledges the support from the Beijing Natural Science Foundation (No. 1194023) and the National Natural Science Foundation of China (NSFC) through the grant 11903005. This work has made use of data from the European Space Agency (ESA) mission *Gaia* (https://www.cosmos.esa.int/gaia), processed by the *Gaia* Data Processing and Analysis Consortium (DPAC, https://www.cosmos.esa.int/web/gaia/dpac/consortium). Funding for the DPAC has been provided by national institutions, in particular the institutions participating in the *Gaia* Multilateral Agreement. This publication makes use of data products from the Wide-field Infrared Survey Explorer, which is a joint project of the University of California, Los Angeles, and the Jet Propulsion Laboratory/California Institute of Technology, funded by the National Aeronautics and Space Administration. The national facility capability for SkyMapper has been funded through ARC LIEF grant LE130100104 from the Australian Research Council, awarded to the University of Sydney, the Australian National University, Swinburne University of Technology, the University of Queensland, the University of Western Australia, the University of Melbourne, Curtin University of Technology, Monash University and the Australian Astronomical Observatory. SkyMapper is owned and operated by The Australian National University's Research School of Astronomy and Astrophysics. The survey data were processed and provided by the SkyMapper Team at ANU. The SkyMapper node of the All-Sky Virtual Observatory (ASVO) is hosted at the National Computational Infrastructure (NCI). Development and support the SkyMapper node of the ASVO has been funded in part by Astronomy Australia Limited (AAL) and the Australian Government through the Commonwealth's Education Investment Fund (EIF) and National Collaborative Research Infrastructure Strategy (NCRIS), particularly the National eResearch Collaboration Tools and Resources (NeCTAR) and the Australian National Data Service Projects (ANDS).

REFERENCES

Allard F., Wesemael F., Fontaine G., Bergeron P., Lamontagne R., 1994, AJ, 107, 1565
Altmann M., Edelmann H., de Boer K. S., 2004, A&A, 414, 181
Asplund M., Grevesse N., Sauval A. J., Scott P., 2009, ARA&A, 47, 481
Baran A., 2012, Acta Astron., 62, 179
Baran A., Reed M., Østensen R., Telting J., Jeffery C., 2017, A&A, 597, 95
Baran A., Telting J., Jeffery C., Østensen R., Vos J., Reed M., Vučković M., 2019, MNRAS, 489, 1556
Baran A. et al., 2009, MNRAS, 392, 1092
Baran A. S., Koen C., Pokrzywka B., 2015, MNRAS, 448, 16
Baran A. S., Winans A., 2012, AcA, 62, 343
Baran A. S. et al., 2012, MNRAS, 424, 2686
Brown T. M., Ferguson H. C., Davidsen A. F., Dorman B., 1997, ApJ, 482, 685

Charpinet S., Fontaine G., Brassard P., Chayer P., Rogers F. J., Iglesias C. A., Dorman B., 1997, ApJ, 483, 123
Charpinet S., Fontaine G., Brassard P., Dorman B., 2000, ApJS, 131, 223
Charpinet S., Giammichele N., Zong W., Grootel V. V., Brassard P., Fontaine G., 2018, Open Astron., 27, 112
Charpinet S., Van Grootel V., Brassard P., Fontaine G., Green E. M., Randall S. K., EPJ Web of Conferences, 2013, 43, 04005
Charpinet S. et al., 2019, A&A, 632, 90
Cutri R. M. et al., 2012, VizieR Online Data Catalog: WISE All-Sky Data Release (Cutri+ 2012), VizieR Online Data Catalog, 2311
de Boer K., 1985, A&A, 142, 321
Dorman B., Rood R. T., O'Connell R. W., 1993, ApJ, 419, 596
Dziembowski W., 1977, Acta Astron., 27, 203
Fitzpatrick E. L., 1999, PASP, 111, 63
Fontaine G., Brassard P., Charpinet S., Green E. M., Randall S. K., Van Grootel V., 2012, A&A, 539, 12
Foster H., Reed M. D., Telting J. H., Østensen R. H., Baran A. S., 2015, ApJ, 805, 94
Gaia Collaboration, 2018, A&A, 616, A1
Geier S., Heber U., Edelmann H., Morales-Rueda L., Kilkenny D., O'Donoghue D., Marsh T. R., Copperwheat C., 2013, A&A, 557, A122
Ghasemi H., Moravveji E., Aerts C., Safari H., Vučković M., 2017, MNRAS, 465, 1518
Graham J. A., Slettebak A., 1973, AJ, 78, 295
Green R. F., Schmidt M., Liebert J., 1986, ApJS, 61, 305
Han Z., Podsiadlowski P., Maxted P. F. L., Marsh T. R., Ivanova N., 2002, MNRAS, 336, 449
Heber U., 2016, PASP, 128, 2001
Heber U., Hunger K., Jonas G., Kudritzki R. P., 1984, A&A, 130, 119
Heber U., Irrgang A., Schaffenroth J., 2018, Open Astron., 27, 35
Heber U., Reid I. N., Werner K., 2000, A&A, 363, 198
Henden A. A., Levine S., Terrell D., Welch D. L., 2015, American Astronomical Society Meeting Abstracts, Vol. 225, #R336.16
Holdsworth D. L., Østensen R. H., Smalley B., Telting J. H., 2017, MNRAS, 466, 5020
Kaluzny J., Ruciński S. M., 1993, MNRAS, 265, 34
Kawaler S., 1988, in Proc. IAU Symp. 123, Advances in Helio- and Asteroseismology. Kluwer, Dordrecht, p. 329
Kilkenny D., Koen C., O'Donoghue D., Stobie R. S., 1997, MNRAS, 285, 640
Lamontagne R., Demers S., Wesemael F., Fontaine G., Irwin M. J., 2000, AJ, 119, 241
Landolt A. U., 2007, AJ, 133, 2502
Lindegren L., 2018, Re-normalising the astrometric chi-square in Gaia DR2, GAIA-C3-TN-LU-LL-124, Lund Observatory
Martin P., Jeffery C. S., Naslim N., Woolf V. M., 2017, MNRAS, 467, 68
Massey P., 1997, A User's Guide to CCD Reductions with IRAF, National Optical Astronomy Observatory
Massey P., Valdes F., Barnes J., 1992, A User's Guide to Reducing Slit Spectra with IRAF, IRAF User Guide 2
Mermilliod J. C., Mermilliod M., Hauck B., 1997, A&AS, 124, 349
Moehler S., 2001, PASA, 113, 1162
Moni Bidin C., Catelan M., Villanova S., Piotto G., Altmann M., Momany Y., Moehler S., 2008, in Heber U., Jeffery C. S., Napiwotzki R., eds, Binaries among Extreme Horizontal Branch Stars in Globular Clusters, Vol. 392. Astronomical Society of the Pacific Conference Series, p. 27
Napiwotzki R., Green P. J., Saffer R. A., 1999, ApJ, 517, 399
Németh P., Kawka A., Vennes S., 2012, MNRAS, 427, 2180
Østensen R. H., Telting J. H., Reed M. D., Baran A. S., Nemeth P., Kiaeerad F., 2014, A&A, 569, 15
Østensen R. H. et al., 2010, A&A, 513, 6
Paunzen E., 2015, A&A, 580, A23
Paxton B., Bildsten L., Dotter A., Herwig F., Lesaffre P., Timmes F., 2011, ApJS, 192, 3
Paxton B. et al., 2013, ApJS, 208, 4
Paxton B. et al., 2015, ApJS, 220, 15
Paxton B. et al., 2018, ApJS, 234, 34
Paxton B. et al., 2019, ApJS, 243, 10
Reed M. D., Foster H., Telting J. H., Østensen R. H., Farris L. H., Oreiro R., Baran A. S., 2014, MNRAS, 440, 3809
Reed M. D. et al., 2011, MNRAS, 414, 2885
Reed M. D. et al., 2020, MNRAS, 493
Reed M. et al., 2018a, Open Astron., 27, 157
Reed M. et al., 2018b, MNRAS, 483, 2282
Ricker G. R. et al., 2014, Transiting Exoplanet Survey Satellite (TESS), Space Telescopes and Instrumentation 2014: Optical, Infrared, and Millimeter Wave, Vol. 9143. Society of Photo-Optical Instrumentation Engineers (SPIE), p. 556
Saffer R. A., Bergeron P., Koester D., Liebert J., 1994, ApJ, 432, 351
Schlafly E. F., Finkbeiner D. P., 2011, ApJ, 737, 103
Schlegel D. J., Finkbeiner D. P., Davis M., 1998, ApJ, 500, 525
Schneider D., Irrgang A., Heber U., Nieva M. F., Przybilla N., 2018, A&A, 618, A86
Silvotti R., Ostensen R. H., Telting J. H., 2019, No close companions to a sample of bright sdB stars. Zenodo, preprint (arXiv:2002.04545)
Silvotti R., Uzundag M., Baran A. S., Østensen R. H., Telting J. H., Heber U., Reed M. D., Vuckovic M., 2019, MNRAS, 489, 4791
Skrutskie M. F. et al., 2006, AJ, 131, 1163
Slettebak A., Brundage R. K., 1971, AJ, 76, 338
Telting J. H. et al., 2012, A&A, 544, 1
Telting J. H. et al., 2014, A&A, 570, 129
Tody D., 1986, in Crawford D. L., ed., The IRAF Data Reduction and Analysis System, Vol. 627. Society of Photo-Optical Instrumentation Engineers (SPIE), p. 733
Tody D., 1993, in Hanisch R. J., Brissenden R. J. V., Barnes J., eds, IRAF in the Nineties, Astronomical Data Analysis Software and Systems II, Vol. 52. Astronomical Society of the Pacific Conference Series, p. 173
Unno W., Osaki Y., Ando H., Shibahashi H., 1979, Forest Grove, Ore., ISBS, Inc., University of Tokyo Press, Tokyo, p. 330
Uzundag M., Baran A., Østensen R., Reed M., Telting J., Quick B., 2017, A&A, 597, 95
Wesemael F., Fontaine G., Bergeron P., Lamontagne R., Green R. F., 1992, AJ, 104, 203
Wolf C. et al., 2018, PASA, 35, e010
Zong W., Charpinet S., Vauclair G., Giammichele N., Van Grootel V., 2016, A&A, 585, 22

This paper has been typeset from a TEX/LATEX file prepared by the author.